# Supporting Information for "Joint inversion of daily and long-period geomagnetic variations reveals lateral variations in upper mantle and transition zone water content"

**F. D. Munch**[1], **A. V. Grayver**[1], **M. Guzavina**[1], **A. V. Kuvshinov**[1], **A. Khan**[1,2]

[1]Institute of Geophysics, ETH Zurich, Switzerland
[2]Institute of Theoretical Physics, University of Zurich, Switzerland

## Content



## Introduction

Figure S1 summarizes the distribution of permanent geomagnetic observatories used in the source coefficient estimation procedure described in Appendix A. Figure S2 depicts times series of coefficient of determination obtained assuming different set of spherical harmonics coefficients to describe the magnetospheric ring current. We find significant differences in the estimated coefficients of determination for 8, 10, and 13 source coefficients, while only marginal changes are observed when 15 coefficients are used.

Our scheme to estimate of source coefficients requires a priori Earth's conductivity model which consists of a mantle with 1-D conductivity distribution overlaid by a surface layer of known laterally-variable conductance. Figure S3 depicts examples of transfer functions obtained when two different 1-D mantle conductivity profiles are used for the source coefficient estimation. We find that differences in the estimated transfer functions are within experimental uncertainties.

The estimated transfer functions were individually inverted to retrieve the most probable set of conductivity models underneath 20 geomagnetic observatories. Station geographic locations and acronyms are depicted in Figure S4 and detailed in Table S1. Figure S5 illustrates the posterior probability distributions retrieved when inverting daily and long-period signals separately and jointly at a single station (Alice Spring in Australia).

Finally, Figures S6–S8 summarize the quality of the data fit for each geomagnetic observatory considered in this study. Figure S9 shows sampled electrical conductivity profiles retrieved from the joint inversion of ionospheric and magnetospheric transfer functions and best-fitting laboratory-based conductivity profiles for Yoshino-Katsura (YK) database.

Corresponding author: Federico D. Munch, federico.munch@erdw.ethz.ch

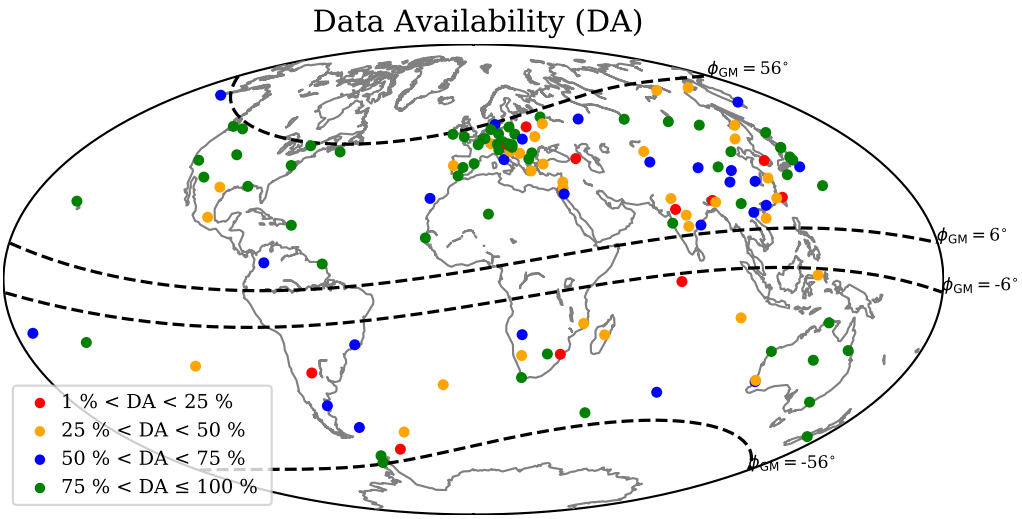


**Figure S1.** Distribution of permanent observatories (geomagnetic latitudes between ±6° and ±55°, shown in figure by dashed lines) used for source coefficient estimation (Section 2.1) color-coded by data availability (DA). DA equal to 100% corresponds to 20 years of data.

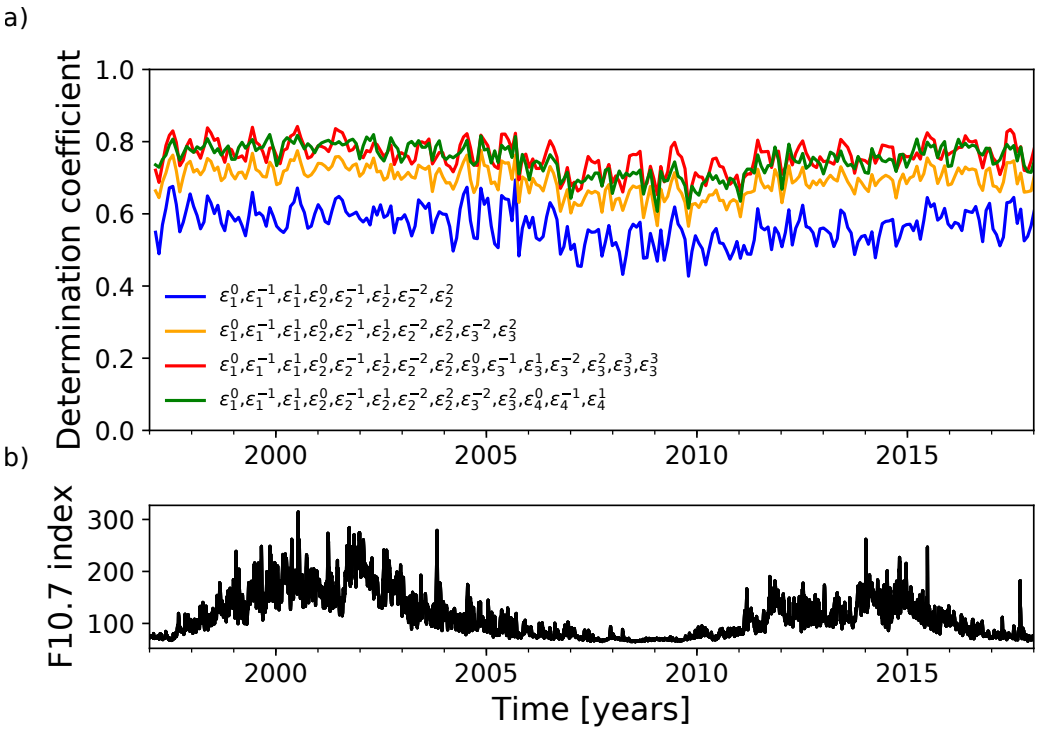


**Figure S2.** (a) Coefficients of determination obtained using different sets of spherical harmonic (SH) coefficients to describe the magnetospheric ring current. (b) Time series of F10.7 index (extracted from http://lasp.colorado.edu/lisird/data/noaa_radio_flux/), which is a proxy for solar activity. We find a good correlation between the coefficients of determination and F10.7 index reflecting that magnetospheric source is stronger during magnetically-active years.

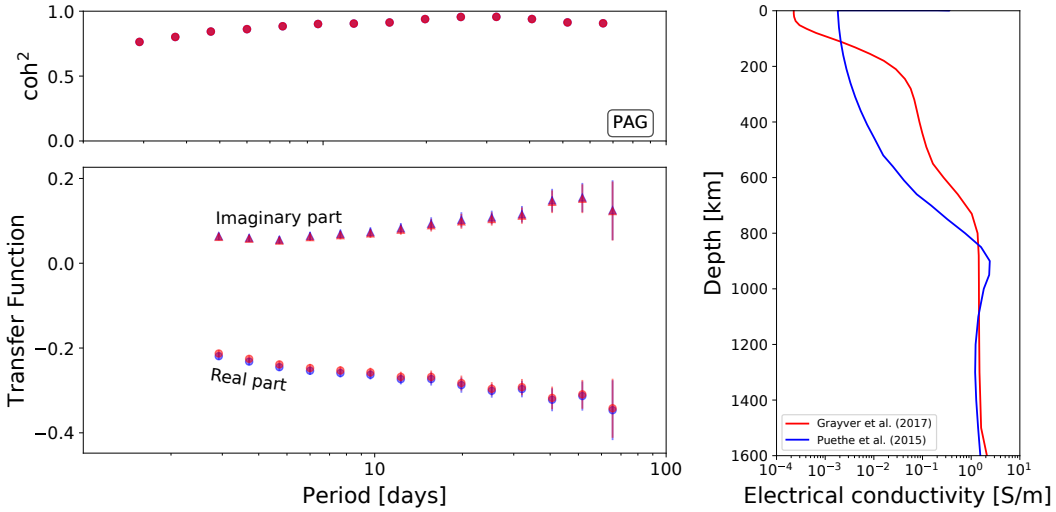


**Figure S3.** Left: Squared coherencies (top) and real (circles) and imaginary (triangles) parts of the transfer functions (bottom) obtained when two different mantle 1-D conductivity profiles (shown in the right plot) were used for the source coefficients estimation. The results are for the observatory Panagyurishte (PAG). Differences in the estimated transfer functions are within observed uncertainties.

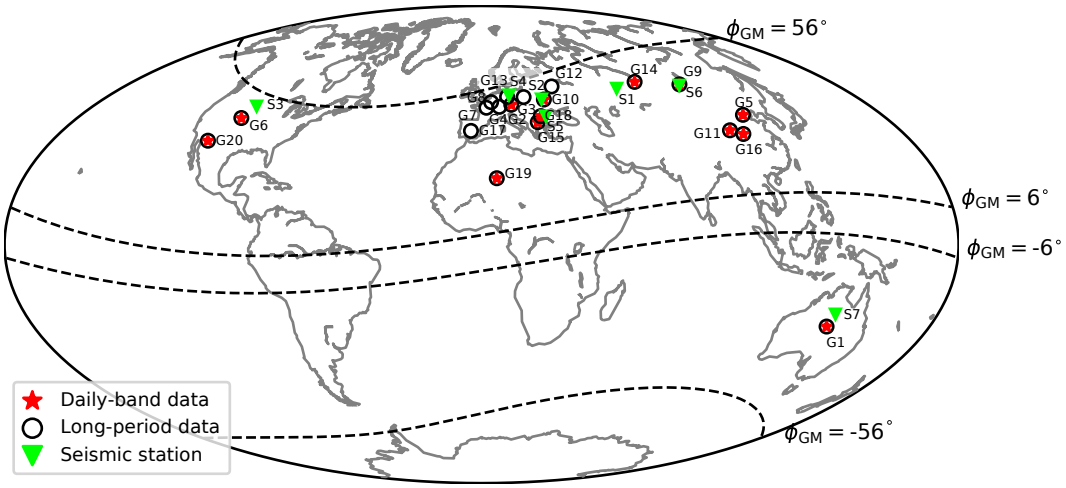


**Figure S4.** Geographic location of mid-latitude observatories (geomagnetic latitudes $\varphi_{GM}$ between ±6° and ±56°) used in this study. Red stars and black circles denote stations at which the observed daily and long-period transfer functions are successfully fitted in the inversion, respectively. Green triangles indicate seismic stations for which constraints on mantle temperature and composition were derived by *Munch et al.* [2019] from analysis of short- and long-period seismic data. Station information is summarized in Table S1. Data fit for all stations are shown in Figures S6–S8.

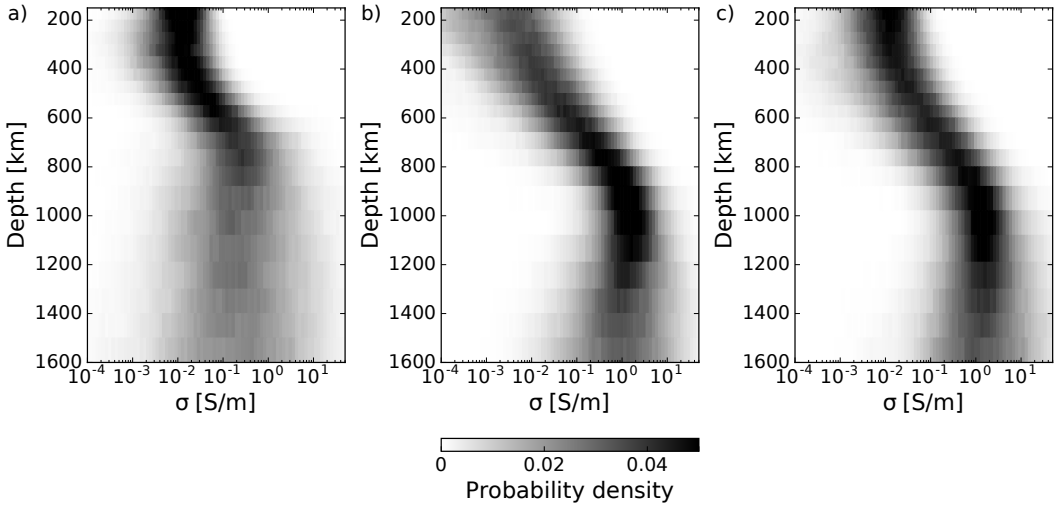


**Figure S5.** Posterior probability distributions for Alice Springs geomagnetic observatory (G1 station in Figure S4) obtained from the inversion of (a) daily transfer functions (TFs), (b) long-period TFs, and (c) daily and long-period TFs, with black indicating most probable and white least probable conductivity models. The posterior probability distributions were determined by computing a histogram of inferred conductivities for each layer assuming a bin-size of 0.05 on the log scale.

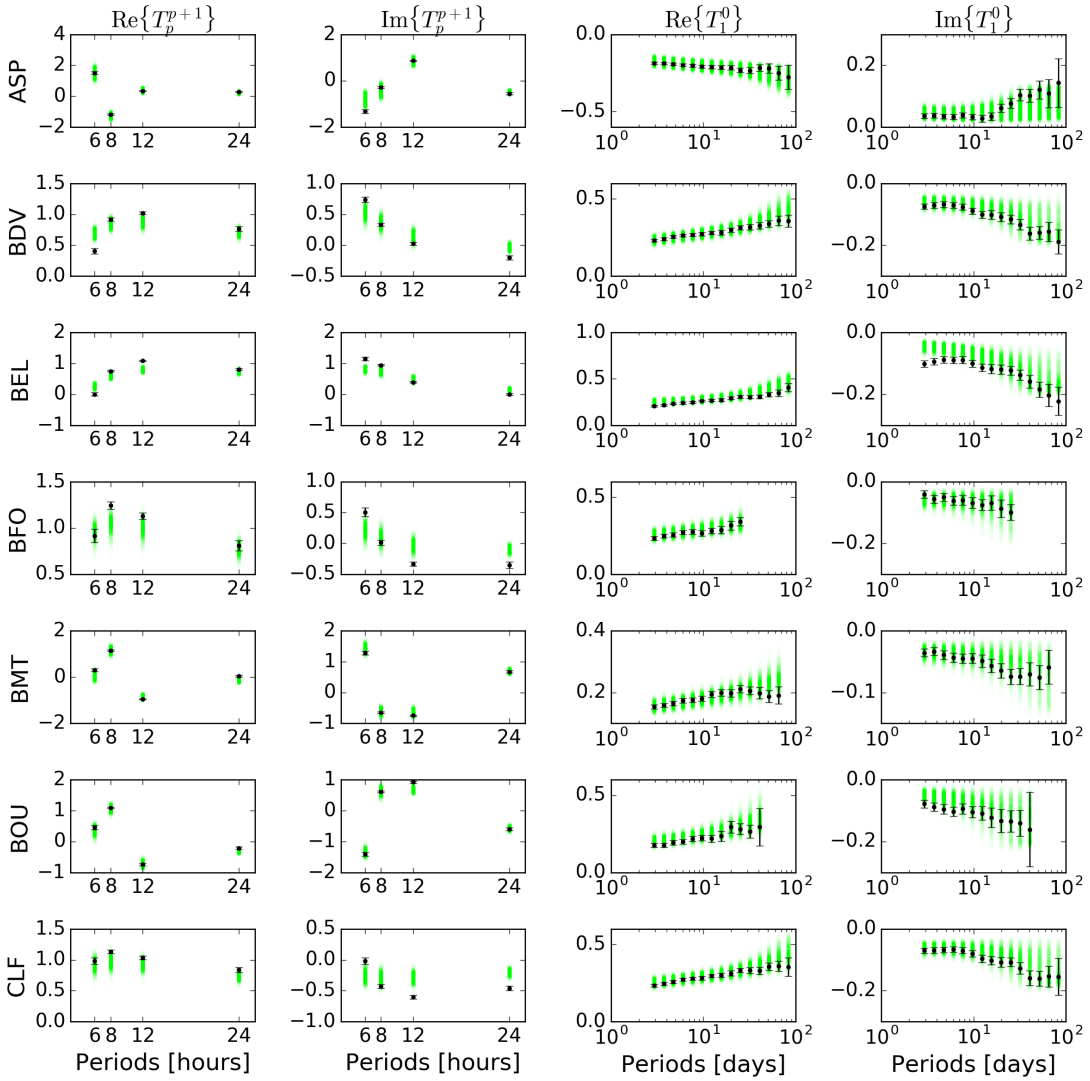


**Figure S6.** Real (Re) and Imaginary (Im) parts of the observed (black) and modelled (green) ionospheric (6–24 hours; left) and magnetospheric (3–85 days; right) transfer functions for Alice Springs (ASP), Budkov (BDV), Belsk (BEL), Black Forest (BFO), Beijing Ming Tombs (BMT), Boulder (BOU), and Chambon la Foret (CLF) geomagnetic observatories. Uncertainties of the observed transfer functions are indicated by the error bars. $p$ runs 1,2, 3 and 4 when period runs 24, 12, 8 and 6 hours respectively.

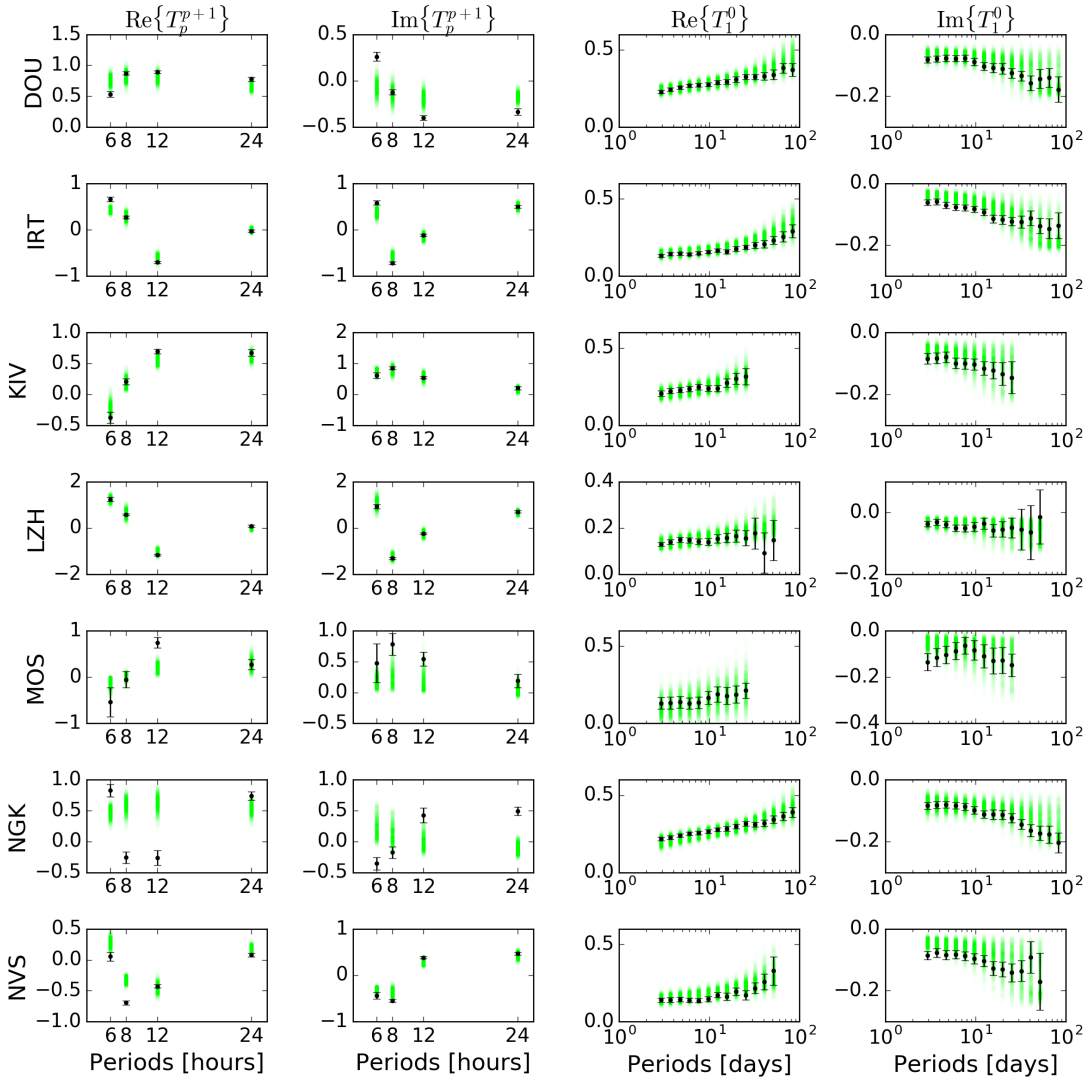


**Figure S7.** Real (Re) and Imaginary (Im) parts of the observed (black) and modelled (green) ionospheric (6–24 hours) and magnetospheric (3–85 days) transfer functions for Dourbes (DOU), Irkutsk (IRT), Kiev (KIV), Lanzhou (LZH), Moscow (MOS), Niemegk (NGK), and Novosibirsk (NVS) geomagnetic observatories. Uncertainties of the observed transfer functions are indicated by the error bars. $p$ runs 1,2, 3 and 4 when period runs 24, 12, 8 and 6 hours respectively.

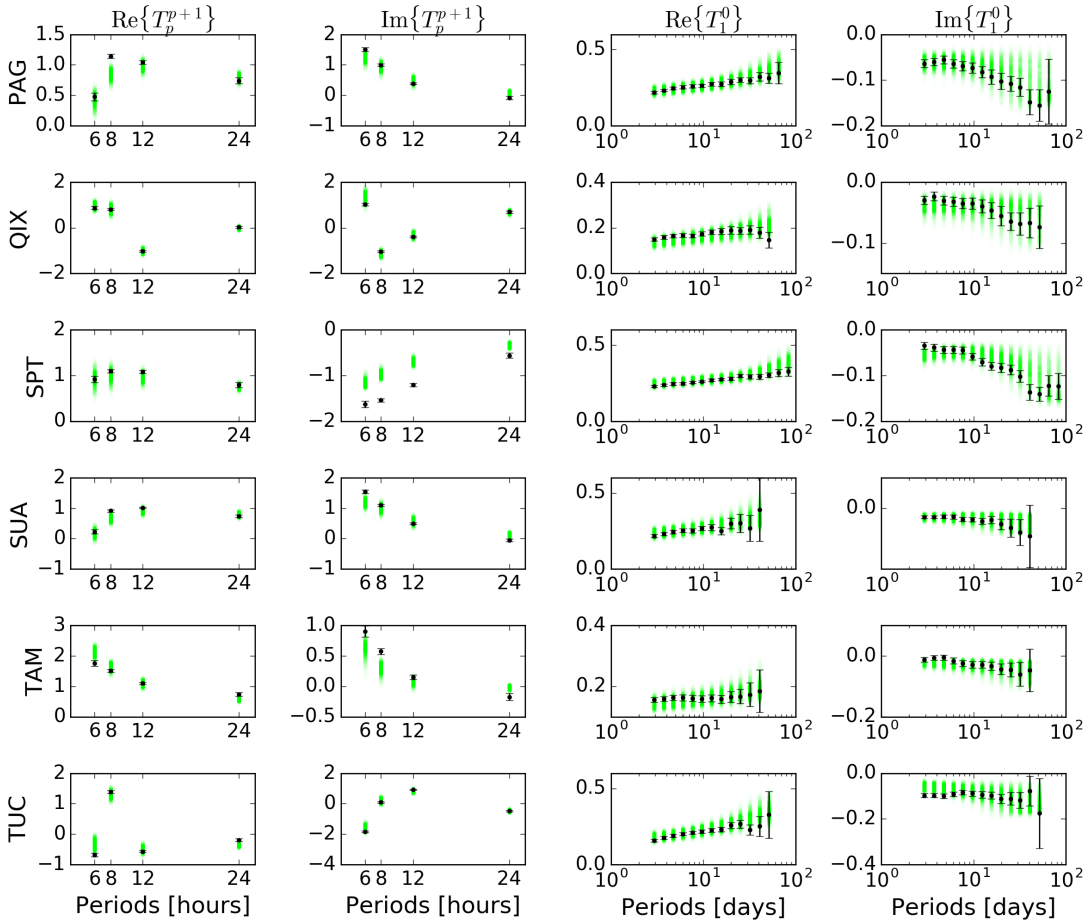


**Figure S8.** Real (Re) and Imaginary (Im) parts of the observed (black) and modelled (green) ionospheric (6–24 hours) and magnetospheric (3–85 days) transfer functions for Panagjurishte (PAG), Qianling (QIX), San Pablo-Toledo (SPT), Surlari (SUA), Tamanrasset (TAM), and Tucson (TUC) geomagnetic observatories. Uncertainties of the observed transfer functions are indicated by the error bars. $p$ runs 1,2, 3 and 4 when period runs 24, 12, 8 and 6 hours respectively.

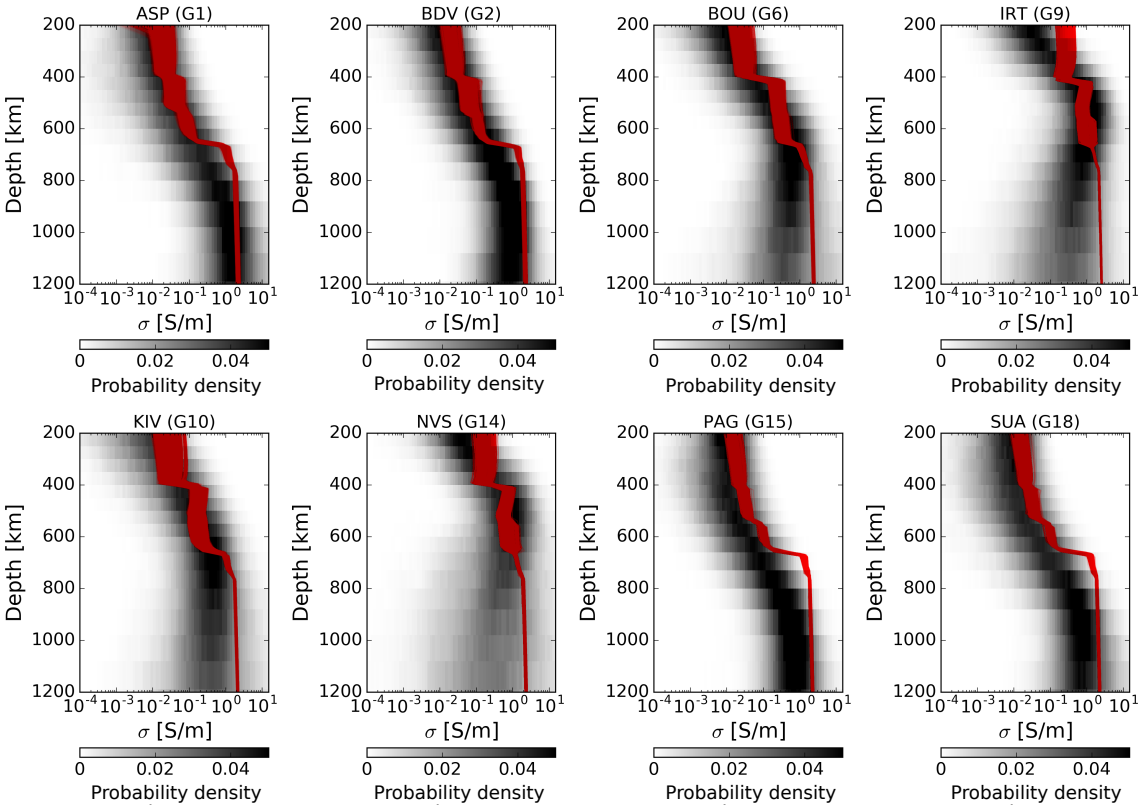


**Figure S9.** Posterior probability density of electrical conductivity ($\sigma$) retrieved from the joint inversion of ionospheric and magnetospheric transfer functions (black) and best-fitting laboratory-based conductivity profiles (red) for YK database. Geographic location of each geomagnetic observatory are shown in Figure 2 and stations acronym are defined in Table 2.

| Code | Acronym | Name | Lat. [°] | Lon. [°] |
|---|---|---|---|---|
| G1 | ASP | Alice Springs | -23.62 | 133.88 |
| G2 | BDV | Budkov | 48.89 | 14.02 |
| G3 | BEL | Belsk | 51.65 | 20.80 |
| G4 | BFO | Black Forest | 48.14 | 8.32 |
| G5 | BMT | Beijing Ming Tombs | 40.11 | 116.20 |
| G6 | BOU | Boulder | 39.94 | -105.23 |
| G7 | CLF | Chambon la Foret | 47.83 | 2.27 |
| G8 | DOU | Dourbes | 49.91 | 4.60 |
| G9 | IRT | Irkutsk | 51.98 | 104.45 |
| G10 | KIV | Kiev | 50.53 | 30.30 |
| G11 | LZH | Lanzhou | 35.90 | 103.85 |
| G12 | MOS | Moscow | 55.29 | 37.32 |
| G13 | NGK | Niemegk | 51.88 | 12.68 |
| G14 | NVS | Novosibirsk | 54.67 | 83.23 |
| G15 | PAG | Panagjurishte | 42.33 | 24.18 |
| G16 | QIX | Qianling | 34.37 | 108.20 |
| G17 | SPT | San Pablo-Toledo | 39.36 | -4.35 |
| G18 | SUA | Surlari | 44.49 | 26.25 |
| G19 | TAM | Tamanrasset | 22.66 | 5.53 |
| G20 | TUC | Tucson | 31.99 | -110.73 |
| S1 | BRVK | Borovoye | 53.06 | 70.28 |
| S2 | KIEV | Kiev | 50.70 | 29.22 |
| S3 | RSSD | Black Hills | 44.12 | -104.04 |
| S4 | RUE | Ruedersdorf | 52.48 | 13.78 |
| S5 | TIRR | Tirgusor | 44.46 | 28.41 |
| S6 | TLY | Talaya | 51.68 | 103.64 |
| S7 | WRAB | Tennant Creek | -19.93 | 134.40 |

**Table S1.** Summary of geomagnetic observatory (G) and seismic station (S) codes, acronyms, names, geographic latitudes, and longitudes.

## References

Munch, F., A. Khan, B. Tauzin, M. van Driel, and D. Giardini (2019), Seismological evidence for the existence of thermo-chemical heterogeneity in Earth's continental mantle, *manuscript under consideration for publication in Nature Geoscience*.